Non-Hermitian topological quantum states in a reservoir-engineered transmon chain

Wojciech Brzezicki,[1,2] Matti Silveri,[3] Marcin Płodzień,[4,2] Francesco Massel,[5] and Timo Hyart[6,7,2]

[1]*Institute of Theoretical Physics, Jagiellonian University, ulica S. Łojasiewicza 11, PL-30348 Kraków, Poland*
[2]*International Research Centre MagTop, Institute of Physics, Polish Academy of Sciences, Aleja Lotników 32/46, PL-02668 Warsaw, Poland*
[3]*Nano and Molecular Systems Research Unit, University of Oulu, FI-90014 Oulu, Finland*
[4]*ICFO - Institut de Ciencies Fotoniques, The Barcelona Institute of Science and Technology, 08860 Castelldefels, Barcelona, Spain*
[5]*Department of Science and Industry Systems, University of South-Eastern Norway, P.O. Box 235, Kongsberg, Norway*
[6]*Computational Physics Laboratory, Physics Unit, Faculty of Engineering and Natural Sciences, Tampere University, FI-33014 Tampere, Finland*
[7]*Department of Applied Physics, Aalto University, 00076 Aalto, Espoo, Finland*

(Received 17 October 2022; revised 15 March 2023; accepted 17 March 2023; published 23 March 2023)

Dissipation in open systems enriches the possible symmetries of the Hamiltonians beyond the Hermitian framework, allowing the possibility of novel non-Hermitian topological phases which exhibit long-living end states that are protected against disorder. So far, non-Hermitian topology has been explored in settings where probing genuine quantum effects has been challenging. We theoretically show that a non-Hermitian topological quantum phase can be realized in a reservoir-engineered transmon chain. The spatial modulation of dissipation is obtained by coupling each transmon to a quantum circuit refrigerator, allowing *in situ* tuning of dissipation strength in a wide range. By solving the many-body Lindblad master equation using a combination of the density matrix renormalization group and Prosen-Seligman third quantization approaches, we show that the topological end modes and the associated phase transition are visible in simple reflection measurements with experimentally realistic parameters. Finally, we demonstrate that genuine quantum effects are observable in this system via robust and slowly decaying long-range quantum entanglement of the topological end modes, which can be generated passively starting from a locally excited transmon.

DOI: 10.1103/PhysRevB.107.115146

I. INTRODUCTION

Non-Hermitian (NH) phenomena in open systems have motivated proposals of new families of topological states [1–10], which have been theoretically predicted to also be applicable to fermionic systems [11–19] and exciton-polariton condensates [20], but the paradigmatic experiments probing the NH topology have so far concentrated on photonic systems, electrical circuits [21–30], spins [31], and cold atoms [32]. So far, the quantum effects of the NH topology have not been extensively explored in these systems. Superconducting circuits, such as arrays of transmon devices [33], are currently used in the most sophisticated attempts to build a scalable quantum computer [34–37] and to simulate electronic properties [38] and topological phases [39,40]. However, their potential in realizing NH topological quantum phases remains to be explored.

In reservoir engineering, the idea is to turn the usually detrimental effects of dissipation into a resource. In this article, we demonstrate that the flexibility to engineer dissipation in a controllable manner in transmon circuits [41–45] can be utilized for realizing NH topological quantum phases. In our proposal, the NH topological phase is created by introducing a spatial modulation of dissipation [7,46] in the one-dimensional Bose-Hubbard transmon chain [47,48], where the dissipation strength in each transmon is controlled by the tunable coupling of the transmon to a quantum circuit refrigerator (QCR) [41–44] (see Fig. 1). In contrast to earlier realizations of NH topological phases, quantum effects are important in transmon circuits and therefore we describe the topological phenomena using the Lindblad master equation approach. By utilizing the third quantization formalism [49], we show that the topology of the Liouvillian superoperator in the noninteracting limit is described by a Chern number [7], which determines the number of topological end modes. We discuss the signatures of the topological end modes and topological phase transition in the reflection measurements, and we utilize the density matrix renormalization group (DMRG) approach to show that the effects of the nontrivial topology can be robustly measured in the presence of a realistic Hubbard interaction caused by the charging energy of the transmons [47,48]. Finally, we show that the quantum nature of the NH topological state can be unambiguously demonstrated by utilizing the topologically protected end modes for the generation of a long-range entangled state from a local excitation of a single transmon. Importantly, we obtain robust entanglement between the transmons at the opposite ends of the chain by just switching on the couplings of the transmons and QCRs, instead of actively controlling the system with a sequence of pulses.

II. NON-HERMITIAN TOPOLOGICAL PHASE IN A TRANSMON CHAIN

The Lindblad master equation for a chain of L transmons in the rotating frame, as demonstrated in Appendix A, can be

 ©2023 American Physical Society

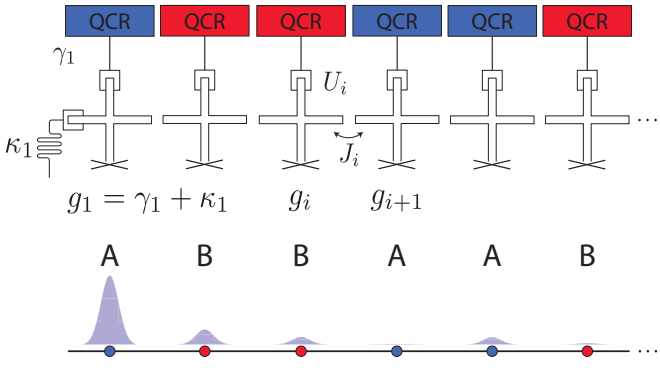

FIG. 1. Schematic illustration of the NH Bose-Hubbard transmon chain for the ABBA configuration. Top: Each transmon is described by the resonance frequency ω_i and the anharmonicity U_i determining the on-site energy and the Hubbard interaction strength for the bosons. The hopping J_i of the bosons between the lattice sites is determined by the capacitive dipole-dipole interaction between the neighboring transmons. The dissipation strength $g_i = (\gamma_i + \kappa_i)/2$ at each lattice site is caused by the coupling of the transmon to the measurement circuit κ_i and the tunable loss caused by the QCR γ_i. Bottom: Site population of the topologically protected state for $g_A = 0.1J$ and $g_B = 3J$. Given the symmetry of the setup, only the six leftmost sites of the 12-site system are depicted.

written as

$$\frac{d\rho}{dt} = \mathcal{L}\rho, \tag{1}$$

where, at zero temperature, the Liouvillian superoperator $\mathcal{L}$ acting on the density matrix ρ is

$$\mathcal{L} = -i[\mathcal{H}\square - \square\mathcal{H}] + \sum_{j=1}^{L} g_j(2a_j\square a_j^\dagger - a_j^\dagger a_j\square - \square a_j^\dagger a_j), \tag{2}$$

where, in the empty squares, one should put the density matrix to get the action of $\mathcal{L}$ on ρ. Here, $\mathcal{H}$ is the Bose-Hubbard Hamiltonian [47,48],

$$\mathcal{H} = \vec{a}^\dagger \hat{H}\vec{a} + \vec{a}^\dagger \vec{f} + \vec{f}^\dagger \vec{a} - \sum_{j=1}^{L} \frac{U_j}{2} a_j^\dagger a_j(a_j^\dagger a_j - 1), \tag{3}$$

$\hat{H}$ is the tight-binding Hamiltonian with number-valued matrix elements H_{ij} $(i, j = 1, 2, \ldots, L)$, and $\vec{a} = (a_1, a_2, \ldots, a_L)$ are operator-valued vectors living in the Fock space. The on-site energies $H_{i,i} = \omega_i - \omega$ are determined by the driving frequency ω and the resonance frequencies of the transmons $\omega_i \approx \sqrt{8E_{C,i}E_{J,i}}$ ($E_{J,i}$ is the flux-tunable Josephson energy and $E_{C,i}$ is the charging energy of the transmon) [33] and the hoppings $H_{i,i+1} = H_{i+1,i} = J_i$ originate from the capacitive dipole-dipole interaction between the neighboring transmons. Additionally, the Hubbard-interaction strength $U_i \approx E_{C,i}$ is caused by the anharmonicity of the transmons [33], the driving strength $f_j = -i\sqrt{\kappa_j}\alpha_j^{\text{in}}$ is determined by the amplitude of the incoming signal α_j^{in} and the coupling of the transmon to the measurement circuit κ_i, and the dissipation strength $g_i = (\gamma_i + \kappa_i)/2$ is mainly controlled by the tunable loss γ_i caused by the QCR. We use notations where $\vec{x}$ indicates a column vector, $\hat{X}$ is a matrix, and a_i are the bosonic annihilation operators. We have set $\hbar = 1$ and assumed the zero-temperature limit for simplicity.

The steady-state output field amplitudes α_j^{out} and the input field amplitudes α_j^{in} are related as

$$\alpha_j^{\text{out}} = \alpha_j^{\text{in}} + \sqrt{\kappa_j}\text{Tr}(a_j\rho_S), \tag{4}$$

where ρ_S is the steady-state solution of Eq. (1). In the linear response regime, the relationship between the $\vec{\alpha}^{\text{out}}$ and $\vec{\alpha}^{\text{in}}$ can be rewritten with the help of a transmission and reflection matrix $\hat{\Gamma}$,

$$\vec{\alpha}^{\text{out}} = \hat{\Gamma}\vec{\alpha}^{\text{in}}. \tag{5}$$

Additionally, we also consider nonlinear responses of the transmons i to a strong driving on one of the transmons j by computing the ratios $\alpha_i^{\text{out}}/\alpha_j^{\text{in}}$. These transmission and reflection amplitudes are directly measurable in the transmon circuits and allow the detection of the topological end modes and phase transition (see below).

The Liouvillian superoperator contains operators acting from left and right on the density matrix, which we denote with superscripts L and R. The Prosen-Seligman third quantization [49] of the Liouvillian superoperator is based on the definition of new operators $\vec{a}_0 = \vec{a}^L$, $(\vec{a}_0')^T = \vec{a}^{L\dagger} - \vec{a}^{R\dagger}$, $(\vec{a}_1)^T = \vec{a}^{R\dagger}$, and $\vec{a}_1' = \vec{a}^R - \vec{a}^L$, which satisfy the usual commutation relations of bosonic annihilation and creation operators; see Appendix B. Using these definitions, the Liouvillian superoperator can be written as

$$\begin{aligned}\mathcal{L} = &-i(\vec{a}_0')^T\hat{H}_{NH}\vec{a}_0 + i(\vec{a}_1')^T\hat{H}_{NH}^*\vec{a}_1 - i(\vec{a}_0')^T\vec{f} + i\vec{f}^\dagger\vec{a}_1' \\ &- i\sum_j \frac{U_j}{2}(2a_{1,j}'a_{1,j}a_{1,j}a_{0,j} + a_{1,j}'a_{1,j}'a_{1,j}a_{1,j} \\ &- a_{0,j}'a_{0,j}'a_{0,j}a_{0,j} - 2a_{0,j}'a_{1,j}a_{0,j}a_{0,j}),\end{aligned} \tag{6}$$

where the non-Hermitian Hamiltonian is defined as

$$\hat{H}_{NH}(\omega) = \hat{H}(\omega) - i\text{diag}(\vec{g}). \tag{7}$$

In the linear response regime, the interaction effects can be neglected and we obtain, as shown in Appendix D,

$$\hat{\Gamma}(\omega) = i\sqrt{\hat{K}}\hat{H}_{NH}(\omega)^{-1}\sqrt{\hat{K}} + \hat{I}_{L\times L}, \tag{8}$$

where $\hat{I}_{L\times L}$ is the identity matrix and $\hat{K} = \text{diag}(\vec{\kappa})$. In the following, we assume that all the transmons have similar resonance frequencies $\omega_i = \omega_0$ and couplings $J_i = J$. This means that the Hermitian part of the $\hat{H}_{NH}$ describes a trivial tight-binding model with constant on-site energies. On the other hand, we assume that the dissipation g_i is spatially modulated. For simplicity, we assume that $\kappa_i = \kappa$, so that the spatial modulation of g_i originates purely from the tunable losses γ_i caused by the QCRs. In the presence of an arbitrary dissipation modulation, this model always satisfies a NH chiral symmetry $\mathcal{S}[\hat{H}_{NH}^\dagger - (\omega_0 - \omega)\hat{I}_{L\times L}]\mathcal{S} = -[\hat{H}_{NH} - (\omega_0 - \omega)\hat{I}_{L\times L}]$, where $\mathcal{S} = \hat{I}_{L/2\times L/2} \otimes \sigma_z$ and the Pauli matrices are denoted as σ_i $(i = x, y, z)$. Therefore, the topology of $\hat{H}_{NH}$ is determined by the Chern number C [7] (see Appendix C), which determines the number of topologically protected end modes at the transmon resonance frequency

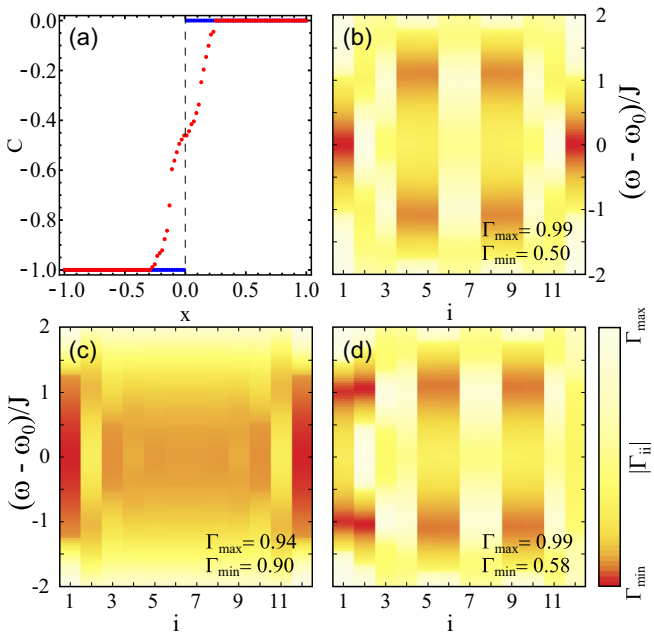

FIG. 2. (a) Topological phase diagram as a function of dissipation strengths interpolating between the ABBA ($x = -1$, $C = -1$) and AABB ($x = 1$, $C = 0$) pattern [Eq. (9)]. In the clean limit, the topological phase transition takes place at $x = 0$ (blue), and the disorder influences the topology only close to $x = 0$ (red). We have used a supercell containing 20 transmons and taken the disorder average of C over 100 disorder realizations. The disorder in J_i (g_i) is sampled from a uniform distribution in the interval $[-\delta J, \delta J]$ ($[-\delta g, \delta g]$). We have used $g_A = 0.1J$, $g_B = 3.0J$, $\delta J = 0.1J$, and $\delta g = 0.29J$. (b)–(d) Contour maps of the reflection coefficients $|\Gamma_{ii}(\omega)|$ in the linear response regime [Eq. (8)] as a function of lattice site i and frequency ω in the nontrivial, gapless and trivial phases. (b) In the nontrivial phase with $x = -1$, the topological end modes show up as a dip in $|\Gamma_{ii}(\omega)|$ at the resonance frequency of the transmon $\omega = \omega_0$ close to the ends of the chain. (c) At the transition ($x = 0$), the bulk is gapless, leading to features in $|\Gamma_{ii}(\omega)|$ at most of the lattice sites in a wide range of frequencies ω around ω_0. (d) In the trivial phase with $x = 1$, the resonant features in the $|\Gamma_{ii}(\omega)|$ are absent at frequencies inside the gap around $\omega = \omega_0$.

$\omega = \omega_0$. In general, it is possible to construct one-dimensional NH models where C takes all possible integer values [17], but, for simplicity, we concentrate here on the simplest models with $|C| =: 0, 1$ [7]. For this purpose, we consider a unit cell consisting of four transmons repeating periodically along the chain. Based on Ref. [7], we know that $C = -1$ for the ABBA pattern of dissipation, whereas $C = 0$ for the AABB pattern of dissipation. Thus, we can interpolate between the topologically distinct phases by assuming

$$g_{1,3}(x) = [g_A + g_B \pm (g_A - g_B)|x|]/2,$$
$$g_{2,4}(x) = [g_A + g_B \pm (g_A - g_B)x]/2. \quad (9)$$

The phase diagram as a function of x is shown in Fig. 2(a): $C = -1$ for $x < 0$ and $C = 0$ for $x > 0$, so that the phase transition takes place at $x = 0$.

Importantly, in transmons, the resonance frequencies ω_i are flux tunable and, in the state-of-the-art experiments, they can be made equal to each other within relative accuracy of 10^{-5}–10^{-4} [50]. Therefore, the disorder effects in ω_i can be neglected. On the other hand, we expect that the parameters J_i and g_i will contain a significant amount of variation. In Fig. 2(a), we demonstrate that the topological phases are robust even in the presence of strong disorder amplitudes δJ and δg. These types of disorder can destroy the topology only if they are sufficiently strong to induce a bulk gap closing, and therefore they are important only close to the topological phase transition where the topological gap is small.

III. SIGNATURES OF NH TOPOLOGICAL PHASE IN REFLECTION MEASUREMENTS

The localization length of the end modes in the topologically nontrivial phase depends sensitively on the dissipation parameters. Here we fix them to $g_A = 0.1J$ and $g_B = 3J$, so that the topological end modes are strongly localized at the end of the chain and numerical calculations can be performed efficiently using a short chain of length $L = 12$. We also set $\kappa = 2g_A$ so that the minimal values of the dissipation originate from the measurement circuits. We use these parameters everywhere in the manuscript unless otherwise stated.

The topological phase diagram shown in Fig. 2(a) can be probed by measuring the reflection $|\Gamma_{ii}(\omega)|$ as a function of lattice site i and frequency ω [see Figs. 2(b)–2(d)]. In the nontrivial phase, the topological end modes show up as a dip in $|\Gamma_{ii}(\omega)|$ at the resonance frequency of the transmon $\omega = \omega_0$ on lattice sites i close to the ends of the chain [see Fig. 2(b)], whereas such kinds of features are absent in the trivial phase where the system is gapped around $\omega = \omega_0$ [see Fig. 2(d)]. At the transition, the bulk is gapless, leading to a broad feature in $|\Gamma_{ii}(\omega)|$ as a function of ω at most of the lattice sites [see Fig. 2(c)].

IV. ROBUSTNESS OF THE TOPOLOGICAL STATES IN THE PRESENCE OF INTERACTIONS

In the limit of weak driving, where the interactions between the bosons can be neglected owing to the small on-site population, the properties of the steady-state system are completely determined by $\hat{H}_{NH}$, and the expectation values of the normal ordered products of the bosonic annihilation and creation operators separate into products of the expectation values; see Appendix E. On the other hand, in the presence of strong driving, the steady state of the interacting system is a correlated quantum state with entanglement between the transmons. We have utilized a generalization of the DMRG approach, described in Appendix F, to describe the steady-state density matrix of the driven system. This allows us to numerically compute the density profile $n_i = \mathrm{Tr}(a_i^\dagger a_i \rho_S)$ and the reflection coefficients $\alpha_i^{\mathrm{out}}/\alpha_i^{\mathrm{in}}$, and representative results of our numerical calculations are shown in Fig. 3. Importantly, we find that the resonant feature of the topological end modes at $\omega = \omega_0$ is very robust in the presence of strong driving and interactions $U_j = U$. Note that despite interaction U being twice the bandwidth, the main dip of $|\Gamma_{ii}(\omega)|$ remains very close to ω_0 even for large driving strength, as shown in Appendix F. Therefore, we argue that the peak originates from the end states present in the noninteracting case that remain robust in the presence of the interactions. Additionally, the

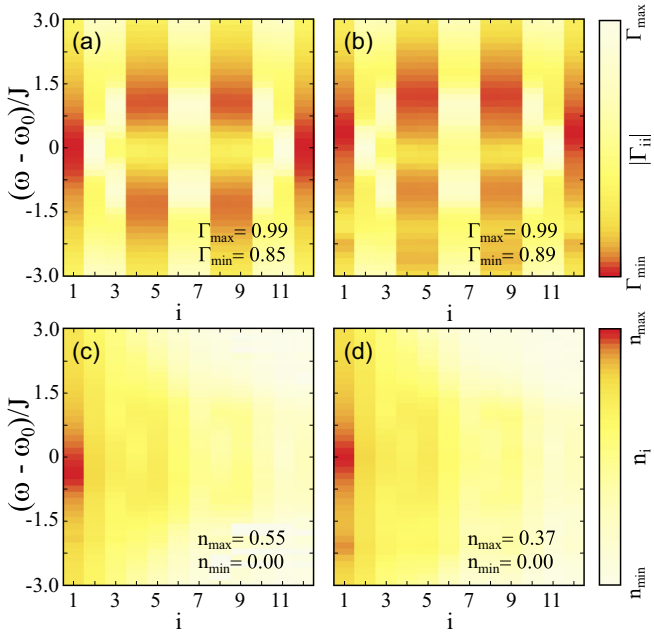

FIG. 3. Contour maps of the reflection coefficients $\Gamma_{ii}(\omega) = \alpha_i^{\text{out}}/\alpha_i^{\text{in}}$ and density $n_i = \text{Tr}(a_i^\dagger a_i \rho_S)$ in a topologically nontrivial chain [$x = -1$ in Eq. (9)] as a function of lattice site i and frequency ω. The driving strength is $|f| = 0.4J$ and the interaction strengths are (a), (c) $U = 1J$ and (b), (d) $U = 4J$. In (a), (b), ρ_S is solved in each case separately when the driving is applied at the different sites i. In (c), (d), the driving is always applied at site 1. In addition to the topological end modes at $\omega \approx \omega_0$, there exist multiboson satellite features at frequencies $\omega \approx \omega_0 - nU/2$ ($n \in \mathbb{Z}$).

topological end modes give rise to satellite features at frequencies $\omega \approx \omega_0 - nU/2$ ($n \in \mathbb{Z}_+$) corresponding to multiboson excitations of the interacting system. See Appendix F for the line plots of the reflection coefficients and the off-diagonal reflection coefficients $|\Gamma_{1i}(\omega)|$.

V. DYNAMICAL GENERATION OF LONG-RANGE ENTANGLEMENT

While the interactions U are not important for the existence of the topological excitations, they offer interesting new possibilities in the utilization of the topological end modes for the generation of entangled quantum states. Namely, in the absence of U, the driving initializes the system to a sitewise product of coherent states, and it turns out that in this case, there is no entanglement between the transmons developing during the time evolution of the density matrix described by Eq. (1), as shown in detail in Appendix G. On the other hand, it is well known that the anharmonicity of the transmons $U \neq 0$ can be utilized for initializing a transmon into a Fock state [51,52]; see Appendix I. To demonstrate that in this case it is possible to create a long-range entangled state, we consider a protocol where the system is initialized to a Fock state with N bosons in a single transmon in the middle of the chain at $t = 0$ and the dissipation strengths are switched on at time $t = t_0$. The dissipation can be controlled fast using the QCRs [41–44], and thus for simplicity we assume that the

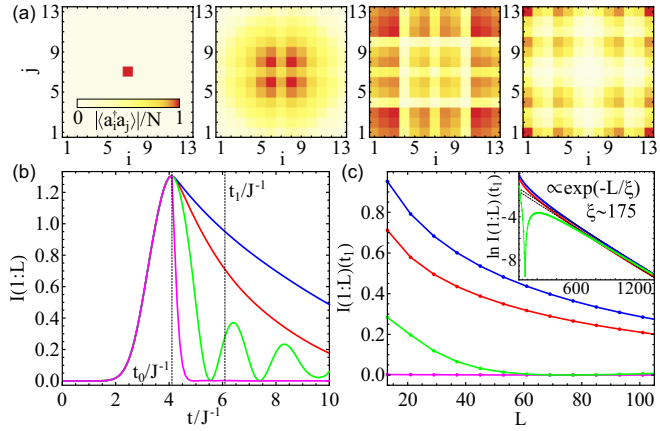

FIG. 4. (a) $\text{Tr}[a_i^\dagger a_j \rho_S(t)]$ vs i and j in the presence of time-dependent dissipation with $x = -1$ in Eq. (9), and $g_{B,\max} = 10J$ and $t_0 \simeq 4.1J^{-1}$ in Eq. (10). The time instants are $t/J^{-1} =: 0, 1, 3, 10$, from left to right. (b) Mutual information $I(1:L)$ vs t for a reference system with uniform dissipation $g_{B,\max} = 0.01J$ (green), trivial phase with $x = 1$ and $g_{B,\max} = 5J$ (magenta), and nontrivial phase with $x = -1$ and $g_{B,\max}/J =: 5, 10$ (red, blue). (c) $I(1:L)$ for the same dissipation profiles as a function of L at time $t_1 = t_0 + 2J^{-1}$, where $I(1:L)(t)$ is maximized at $t = t_0$. The logarithmic plot is shown in the inset. In addition to the dissipation patterns (9), we have added one extra site in the middle of the chain with $g_{L/2+1} = g_B$, which is excited to a Fock state with $N = 5$ at $t = 0$.

time dependence of the dissipation parameters is given by

$$g_A = 0.01J, \; g_B = \begin{cases} 0.01J, & t \leqslant t_0 \\ g_{B,\max}, & t > t_0. \end{cases} \tag{10}$$

We assume that the other transmons have sufficiently small U so that the interactions can be neglected during the time evolution. In Fig. 4(a), we show the time evolution of the expectation values $\text{Tr}[a_i^\dagger a_j \rho_S(t)]$ in the case of a topologically nontrivial dissipation pattern. It demonstrates that there exists a quasistable (slowly decaying) state, where the bosons are dominantly trapped at the end of the chain. We can characterize the entanglement between the end transmons 1 and L with the help of time-dependent mutual information $I(1:L)(t)$ (see Appendix H for details), and we find that in the case of a topologically nontrivial NH phase, the generated entanglement is more stable in time than in the reference cases of trivial and uniform chains [Fig. 4(b)]. Furthermore, the entanglement decreases only slowly with the increasing length of the chain [Fig. 4(c)]. The final state can read out by means of two-transmon tomography that again relies on interaction U, as described in Appendix I.

VI. CONCLUSIONS

To summarize, we have shown that a NH topological quantum phase can be realized in a transmon chain by utilizing a spatial modulation of dissipation obtained by coupling the transmons to QCRs. The topological end modes and topological phase transition can be detected with the reflection measurements, and the effects of the nontrivial topology can be robustly measured in the presence of interactions. Moreover, the topologically protected end modes can be utilized

for the generation of a long-range entangled state from a local excitation of a single transmon, and we expect that in a similar way, a whole family of more complicated entangled states of multiple transmons can be generated by creating suitable spatial patterns of domain walls separating topologically distinct phases. Experiments could also probe the interacting physics in longer chains where the simulations are not computationally feasible. Therefore, our results open interesting directions for future research in the topological initialization of qubits and topological quantum state engineering.

The codes supporting the theory are available from W.B. upon reasonable request.

ACKNOWLEDGMENTS

We acknowledge the computational resources provided by the Aalto Science-IT project and the financial support from the Academy of Finland Projects No. 331094 and No. 316619. The work is supported by the Foundation for Polish Science through the IRA Programme co-financed by EU within SG OP. W.B. also acknowledges support by Narodowe Centrum Nauki (NCN, National Science Centre, Poland), Project No. 2019/34/E/ST3/00404. M.P. acknowledges the support of the Polish National Agency for Academic Exchange, the Bekker Programme No. PPN/BEK/2020/1/00317, and Ministerio de Ciencia y Innovation Agencia Estatal de Investigaciones (R&D Project No. CEX2019-000910-S, AEI/10.13039/501100011033, Plan National FIDEUA PID2019-106901GB-I00, FPI), Fundació Privada Cellex, Fundació Mir-Puig, and by Generalitat de Catalunya (AGAUR Grant No. 2017 SGR 1341, CERCA program). F.M. acknowledges financial support from the Research Council of Norway (Grant No. 333937) through participation in the QuantERA ERA-NET Cofund in Quantum Technologies (project MQSens) implemented within the European Union's Horizon 2020 Programme.

APPENDIX A: DRIVEN BOSE-HUBBARD HAMILTONIAN IN THE ROTATING FRAME

In the rotating wave approximation, the driven Bose-Hubbard Hamiltonian can be written as

$$\mathcal{H}_{\rm lab} = \sum_{j=1}^{L}\omega_j a_j^\dagger a_j + \sum_{j=1}^{L-1} J_j(a_j^\dagger a_{j+1} + a_{j+1}^\dagger a_j) + \sum_{j=1}^{L}(a_j^\dagger f_j e^{-i\omega t} + a_j f_j^* e^{i\omega t}) - \sum_{j=1}^{L}\frac{U_j}{2}a_j^\dagger a_j(a_j^\dagger a_j - 1), \tag{A1}$$

where ω is the driving frequency. We can now switch to a rotating frame with a time-dependent transformation,

$$\mathcal{U}(t) = \exp\left(-i\omega t\sum_{j=1}^{L} a_j^\dagger a_j\right). \tag{A2}$$

In this way, we obtain the driven Bose-Hubbard Hamiltonian in the rotating frame given in the main text,

$$\begin{aligned}\mathcal{H} &= \mathcal{U}(t)^\dagger \mathcal{H}_{\rm lab}\mathcal{U}(t) - i\,\mathcal{U}(t)^\dagger\frac{d\,\mathcal{U}(t)}{dt}\\ &= \sum_{j=1}^{L}(\omega_j-\omega)a_j^\dagger a_j + \sum_{j=1}^{L-1}J_j(a_j^\dagger a_{j+1} + a_{j+1}^\dagger a_j)\\ &\quad + \sum_{j=1}^{L}(a_j^\dagger f_j + a_j f_j^*) - \sum_{j=1}^{L}\frac{U_j}{2}a_j^\dagger a_j(a_j^\dagger a_j - 1).\end{aligned} \tag{A3}$$

APPENDIX B: THIRD QUANTIZATION OF THE LIOUVILLIAN SUPEROPERATOR

The Liouvillian superoperator contains operators acting from left and right on the density matrix. Therefore, we use notations

$$A^L\rho := A\rho,\ A^R\rho := \rho A. \tag{B1}$$

We are interested in the calculation of expectation values of observables O of the form $\mathrm{Tr}(O\rho)$. Therefore, the above definition allows us also to determine how the right and left operators act on the observables,

$$\begin{aligned}&\mathrm{Tr}(OA^L\rho) = \mathrm{Tr}(OA\rho) \Rightarrow OA^L = OA,\\ &\mathrm{Tr}(OA^R\rho) = \mathrm{Tr}(O\rho A) = \mathrm{Tr}(AO\rho) \Rightarrow OA^R = AO.\end{aligned} \tag{B2}$$

For two operators, we have

$$A^L B^L\rho = AB\rho,\ A^R B^R\rho = \rho BA. \tag{B3}$$

The third quantization is based on new operators $\vec{a}_\nu$ and $\vec{a}'_\nu$ ($\nu = 0, 1$), defined as [49]

$$\begin{aligned}&\vec{a}_0 := \vec{a}^L,\quad (\vec{a}'_0)^T := \vec{a}^{L\dagger} - \vec{a}^{R\dagger},\\ &(\vec{a}_1)^T := \vec{a}^{R\dagger},\quad \vec{a}'_1 := \vec{a}^R - \vec{a}^L.\end{aligned} \tag{B4}$$

The inverse transformation is

$$\begin{aligned}&\vec{a}^L := \vec{a}_0,\quad \vec{a}^{L\dagger} := (\vec{a}'_0)^T + (\vec{a}_1)^T,\\ &\vec{a}^R := \vec{a}_0 + \vec{a}'_1,\quad \vec{a}^{R\dagger} := (\vec{a}_1)^T.\end{aligned} \tag{B5}$$

The calculation of the commutators yields

$$\begin{aligned}&[a_{\nu,j}, a'_{\nu',k}]\Box = \delta_{\nu\nu'}\delta_{jk}\Box,\\ &[a_{\nu,j}, a_{\nu',k}]\Box = 0 = [a'_{\nu,j}, a'_{\nu',k}]\Box.\end{aligned} \tag{B6}$$

Therefore, the operators $\vec{a}_\nu$ and $\vec{a}'_\nu$ act similarly as the bosonic annihilation and creation operators, respectively. Other useful properties of the operators and the density matrix are

$$1\vec{a}'_\nu = 0,\ \ \vec{a}_\nu\rho_0 = 0,\ \ \mathrm{Tr}\rho_0 = 1, \tag{B7}$$

where we have denoted the identity observable with 1 and the density matrix of the vacuum with $\rho_0 = |\vec{0}\rangle\langle\vec{0}|$. In particular, the properties described above allow one to define the dual Fock space for density matrices and observables [49],

$$|\vec{m}\rangle = \prod_{\nu,j}\frac{(a'_{\nu,j})^{m_{\nu,j}}}{\sqrt{m_{\nu,j}!}}\rho_0,\ \ (\vec{m}| = 1\prod_{\nu,j}\frac{(a_{\nu,j})^{m_{\nu,j}}}{\sqrt{m_{\nu,j}!}}, \tag{B8}$$

with bi-orthonormality

$$\mathrm{Tr}(\vec{m}'|\vec{m}\rangle = \delta_{\vec{m}',\vec{m}}. \tag{B9}$$

Within this dual Fock space, the operators $\vec{a}_\nu$ and $\vec{a}'_\nu$ have the matrix representations of the bosonic annihilation and creation operators, respectively. Using these definitions, the Liouvillian superoperator can be written as

$$\begin{aligned}\mathcal{L} = &-i(\vec{a}'_0)^T \hat{H}_{NH}\vec{a}_0 + i(\vec{a}'_1)^T \hat{H}^*_{NH}\vec{a}_1 - i(\vec{a}'_0)^T \vec{f} + i\vec{f}^\dagger \vec{a}'_1 \\ &- i\sum_j \frac{U_j}{2}(2a'_{1,j}a_{1,j}a_{1,j}a_{0,j} + a'_{1,j}a'_{1,j}a_{1,j}a_{1,j}) \\ &+ i\sum_j \frac{U_j}{2}(2a'_{0,j}a_{1,j}a_{0,j}a_{0,j} + a'_{0,j}a'_{0,j}a_{0,j}a_{0,j}),\end{aligned} \tag{B10}$$

where the non-Hermitian Hamiltonian is defined as

$$\hat{H}_{NH} = \hat{H} - i\mathrm{diag}(\vec{g}). \tag{B11}$$

APPENDIX C: TOPOLOGICAL INVARIANT IN THE NONINTERACTING LIMIT $U_i = 0$

In the case of an infinite number of four-site unit cells, $\omega_i = \omega_0$ and $J_i = J$, the topological invariant for the noninteracting non-Hermitian Hamiltonian $\hat{H}_{NH}$ can be written as [7]

$$C = \frac{1}{2\pi}\int_{-\infty}^{+\infty} d\eta \int_0^{2\pi} dk\, \Omega_{k,\eta}, \tag{C1}$$

where

$$\Omega_{k,\eta} = \sum_{\substack{n\leqslant 2\\ m>2}} \mathrm{Im}\frac{2\langle\psi^n_{k,\eta}|\partial_k\hat{H}^{\mathrm{eff}}|\psi^m_{k,\eta}\rangle\langle\psi^m_{k,\eta}|\partial_\eta\hat{H}^{\mathrm{eff}}|\psi^n_{k,\eta}\rangle}{\left(E^{(n)}_{k,\eta} - E^{(m)}_{k,\eta}\right)^2}$$

is the Berry curvature corresponding to the two-dimensional (2D) Hamiltonian

$$\hat{H}^{\mathrm{eff}}(k,\eta) = \begin{pmatrix} \eta - g_1 & -iJ & 0 & -iJe^{-ik} \\ iJ & -\eta + g_2 & iJ & 0 \\ 0 & -iJ & \eta - g_3 & -iJ \\ iJe^{ik} & 0 & iJ & -\eta + g_4 \end{pmatrix}, \tag{C2}$$

with $|\psi^n_{k,\eta}\rangle$ and $E^n_{k,\eta}$ denoting the eigenstates and eigenenergies of $\hat{H}^{\mathrm{eff}}(k,\eta)$ (sorted in ascending order of the eigenenergy). The effective Hermitian Hamiltonian is related with $\hat{H}_{NH}$ by the equation

$$\hat{H}^{\mathrm{eff}}(k,\eta) = \eta\mathcal{S} - i\mathcal{S}[\hat{H}_{NH}(k) - (\omega_0 - \omega)\hat{I}_{4\times 4}], \tag{C3}$$

where $\mathcal{S}$ is a chiral symmetry operator related to $\hat{H}_{NH}$. The physical meaning of the parameter η is that it is the imaginary part of an eigenstate of $\hat{H}_{NH}$ whose real part is zero; see Ref. [7].

APPENDIX D: TRANSMISSION AND REFLECTION MATRIX IN THE LINEAR RESPONSE REGIME

The effects of interactions can be neglected in the linear response regime. By transforming the third-quantized bosonic operators as

$$\vec{a}_\nu = \vec{c}_\nu + \vec{x}_\nu, \qquad \vec{a}'_\nu = \vec{c}'_\nu, \tag{D1}$$

we obtain

$$\mathcal{L} = -i(\vec{c}'_0)^T \hat{H}_{NH}\vec{c}_0 + i(\vec{c}'_1)^T \hat{H}^*_{NH}\vec{c}_1 - i(\vec{c}'_0)^T \vec{f} + i\vec{f}^\dagger \vec{c}'_1. \tag{D2}$$

Therefore, we can get rid of the driving terms by requiring that $\vec{x}_\nu$ ($\nu = 0, 1$) satisfy

$$\vec{x}_0 = -\hat{H}^{-1}_{NH}\vec{f}, \quad \vec{x}_1 = \vec{x}^\star_0. \tag{D3}$$

In this way, we obtain

$$\mathcal{L} = -i(\vec{c}'_0)^T \hat{H}_{NH}\vec{c}_0 + i(\vec{c}'_1)^T \hat{H}^*_{NH}\vec{c}_1. \tag{D4}$$

The Liouvillian superoperator given by Eq. (D4) can be diagonalized,

$$\mathcal{L} = \sum_k [-iE_k b'_{0,k}b_{0,k} + iE^*_k b'_{1,k}b_{1,k}], \tag{D5}$$

using a transformation,

$$\begin{aligned}\vec{c}_0 &= \hat{U}\vec{b}_0,\ (\vec{c}'_0)^T = (\vec{b}'_0)^T\hat{U}^{-1}, \\ \vec{c}_1 &= \hat{U}^*\vec{b}_1,\ (\vec{c}'_1)^T = (\vec{b}'_1)^T(\hat{U}^{-1})^*,\end{aligned} \tag{D6}$$

where the matrix $\hat{U}$ diagonalizes the non-Hermitian Hamiltonian,

$$\hat{U}^{-1}\hat{H}_{NH}\hat{U} = \mathrm{diag}(\vec{E}). \tag{D7}$$

Therefore, the non-Hermitian Hamiltonian fully determines the spectrum of the Liouvillian superoperator. Here, the operators $\vec{b}_\nu$ and $\vec{b}'_\nu$ ($\nu = 0, 1$) satisfy the bosonic commutation relations

$$\begin{aligned}&[b_{\nu,j}, b'_{\nu',k}]\square = \delta_{\nu\nu'}\delta_{jk}\square, \\ &[b_{\nu,j}, b_{\nu',k}]\square = 0 = \left[b'_{\nu,j}, b'_{\nu',k}\right]\square,\end{aligned} \tag{D8}$$

and

$$1\vec{b}'_\nu = 0. \tag{D9}$$

Because all eigenenergies of H_{NH} satisfy $\mathrm{Im}E_k < 0$, there exists a unique steady-state solution of the density matrix ρ_S and its physical properties are determined by the relations

$$b_{\nu,j}\rho_S = 0, \quad \mathrm{Tr}\rho_S = 1. \tag{D10}$$

To compute the output fields,

$$\alpha^{\mathrm{out}}_j = \alpha^{\mathrm{in}}_j + \sqrt{\kappa_j}\mathrm{Tr}(a_j\rho_S), \tag{D11}$$

we need to calculate the expectation values,

$$\begin{aligned}\mathrm{Tr}(a_j\rho_S) &= \mathrm{Tr}(a_{0,j}\rho_S) = \mathrm{Tr}[(c_{0,j} + x_{0,j})\rho_S] = x_{0,j} \\ &= -\left(\hat{H}^{-1}_{NH}\vec{f}\right)_j.\end{aligned} \tag{D12}$$

Using $f_j = -i\sqrt{\kappa_j}\alpha^{\mathrm{in}}_j$, we obtain

$$\vec{\alpha}^{\mathrm{out}} = \hat{\Gamma}(\omega)\vec{\alpha}^{\mathrm{in}}, \quad \hat{\Gamma}(\omega) = i\sqrt{\hat{K}}\hat{H}^{-1}_{NH}\sqrt{\hat{K}} + \hat{I}, \tag{D13}$$

where $\hat{I}$ is the identity matrix and $\hat{K} = \mathrm{diag}(\vec{\kappa})$.

APPENDIX E: EXPECTATION VALUES OF OPERATORS IN THE NONINTERACTING LIMIT

In the noninteracting limit, we can straightforwardly compute the expectation value of an arbitrary normal-ordered

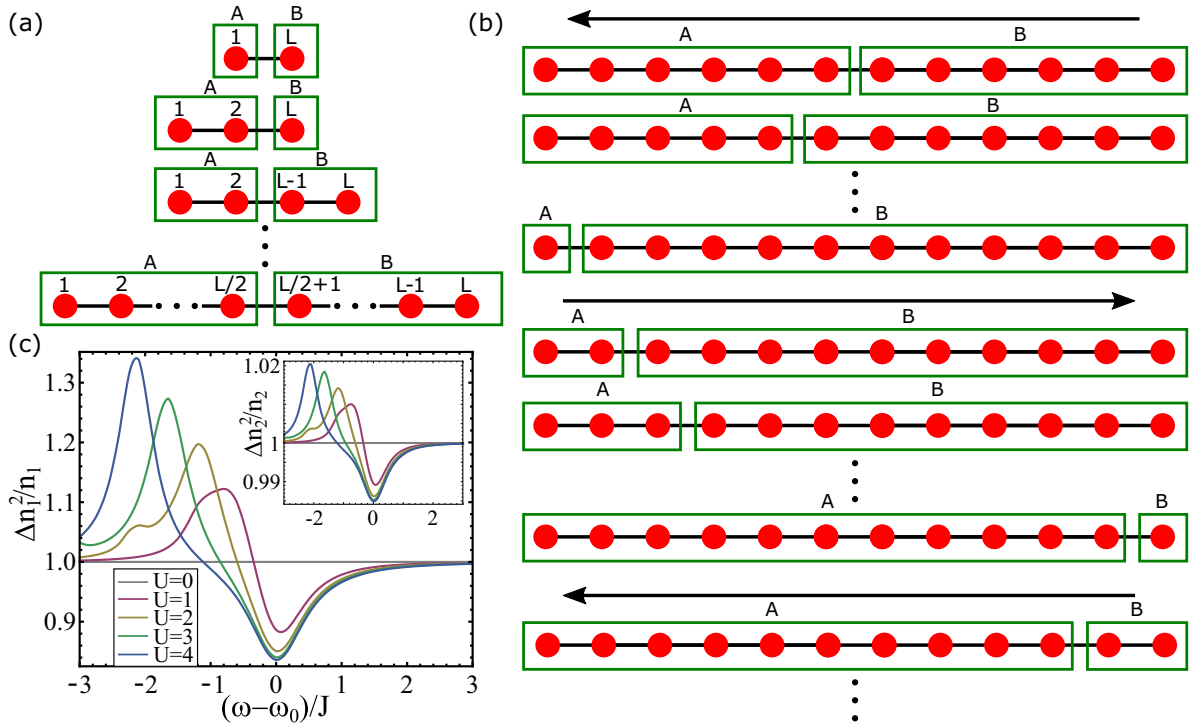

FIG. 5. (a), (b) Schematics of the DMRG. (a) The building of the system by expanding two blocks, A and B. (b) The sweeping loop for a finite open-ends system. (c) The variance of the density $\Delta n_j^2/n_j$ for lattice sites $j = 1$ and $j = 2$ (inset) as functions of frequency ω when the system is driven at the first lattice site for $f = 0.2J$ and $U/J =: 0, 1, 2, 3, 4$.

product of creation and annihilation operators,

$$\begin{aligned}\mathrm{Tr}(a_{i_1}^\dagger \dots a_{i_N}^\dagger a_{j_1} \dots a_{j_M}\rho_S) &= \mathrm{Tr}(a_{1,i_1} \dots a_{1,i_N} a_{0,j_1} \dots a_{0,j_M}\rho_S)\\ &= x_{1,i_1} \dots x_{1,i_N} x_{0,j_1} \dots x_{0,j_M}\\ &= \mathrm{Tr}(a_{i_1}^\dagger \rho_S) \dots \mathrm{Tr}(a_{i_N}^\dagger \rho_S)\\ &\quad \times \mathrm{Tr}(a_{j_1}\rho_S) \dots \mathrm{Tr}(a_{j_M}\rho_S). \quad \text{(E1)}\end{aligned}$$

The expectation value of the product of operators separates into a product of expectation values because, in the third-quantized formulation, the steady state of the system is a product of a coherent state at each lattice site. The expectation values of the other operators can be obtained from this formula by utilizing the commutation relations of the annihilation and creation operators. In particular, it follows from Eq. (E1) that the variance of the density in the steady state $n_j = \mathrm{Tr}(a_j^\dagger a_j \rho_S)$ satisfies

$$\Delta n_j^2 = \mathrm{Tr}(a_j^\dagger a_j a_j^\dagger a_j \rho_S) - [\mathrm{Tr}(a_j^\dagger a_j \rho_S)]^2 = \mathrm{Tr}(a_j^\dagger a_j \rho_S) = n_j, \quad \text{(E2)}$$

and the covariance of the annihilation operators satisfies

$$\mathrm{cov}[a_i, a_j] = \mathrm{Tr}(a_i a_j \rho_S) - \mathrm{Tr}(a_i \rho_S)\mathrm{Tr}(a_j \rho_S) = 0. \quad \text{(E3)}$$

APPENDIX F: DENSITY MATRIX RENORMALIZATION GROUP APPROACH FOR THE INTERACTING PROBLEM

The standard finite-size density renormalization group approach is described in Ref. [53]. Here we use this approach, with a few modifications, to solve the third-quantized Lindblad superoperator of Eq. (B10) for its right zero vector—a nonequilibrium stationary state. First, we need to truncate the local Hilbert space of the boson operators $a_{\nu,j}$ to a finite value which becomes a convergence parameter r. Thus, having fixed r at a certain value, we can have no more than $(r-1)$ third-quantized bosons per site. Now, in a finite Hilbert space, we can always find a (right) zero vector of $\mathcal{L}$: Vacuum is obviously a left zero state of $\mathcal{L}$, meaning that $\det \mathcal{L}^T = \det \mathcal{L} = 0$, so a right zero vector must also exist. The search for it is thus equivalent to finding an eigenvector of $\mathcal{L}$ with zero eigenvalue.

We adapt the general algorithm described in Ref. [53]. In the first stage, we want to increase the system size starting from two sites, $j = 1$ and $j = L$; see Fig. 5(a). These two sites constitute blocks A and B at the first step of the DMRG. Note that we treat $\nu = 0, 1$ as the internal degree of freedom, so each dot in Figs. 5(a) and 5(b) represents two bosonic degrees of freedom so that the dimension of the local Hilbert space at a given site j is equal to r^2. At a given system size, we search for the eigenvector of $\mathcal{L}$ whose eigenvalue is closest to zero using the Arnoldi algorithm. Then, we use singular value decomposition (SVD), as usual in DMRG, and truncate the basis at the cutoff size of d, which is another convergence parameter. Now we expand the blocks by adding sites. Here we choose to do it asymmetrically by adding one site to the right in block A. By doing this, we increase the dimension of the Hilbert space of block A by r^2 and of the whole Hilbert space by r^2 as well. If we decide to do it in a more standard way, by growing two blocks symmetrically, then the dimension grows by a factor of r^4, which is less handleable. In the next step, we add one site to the left of block B and we continue until we reach the desired system size L. All the blocks are stored in

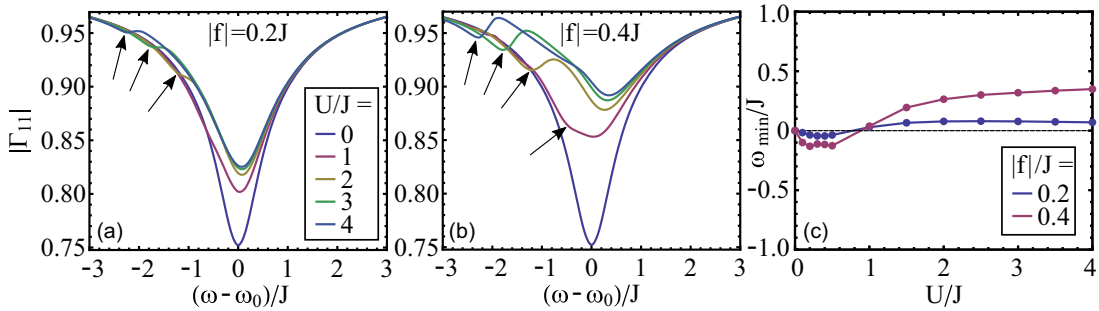

FIG. 6. Reflection coefficient $|\Gamma_{11}(\omega)|$ in the nonlinear response regime as a function of frequency ω in the nontrivial phase ($x = -1$) for interaction strengths $U/J =: 0, 1, 2, 3, 4$ in the case of (a) moderate driving $f = 0.2J$ and (b) strong driving $f = 0.4J$. Multiboson features are marked with arrows. (c) Position of the global minimum of $|\Gamma_{11}(\omega)|$ as function of U for moderate and strong driving.

memory, meaning that one can always recover the Linbladian and any observables for block A or B containing from 1 up to $L/2$ sites.

After obtaining the system in the desired size L, we optimize the stationary state by performing sweeps; see Fig. 5(b). We expand one block and shrink the other each time, asking for the eigenstate with the eigenvalue closest to zero and performing SVD followed by the basis truncation. Shrinking of a block means reading a recorded block of the size that we need. Sweeps are done left and right, as shown in Fig. 5(b), until the eigenvalue of our stationary state $|\rho_S\rangle$ is close enough to zero. Here the important difference with respect to the usual Hermitian case is how we calculate observables. From the third quantization, we get that the stationary-state average of an operator O is given by

$$\mathrm{Tr}(O\rho_S) = \langle 0|O|\rho_S\rangle, \tag{F1}$$

where, in bra, we have vacuum of the $a_{v,j}$ bosons. Thus, to calculate any averages in DMRG, we need to know current representation of the vacuum state. This is not trivial because, from the construction, the converged basis is optimized to represent the stationary state only. Nevertheless, having $\mathcal{L}$ in a truncated basis, we can always ask for the lowest-magnitude eigenvector of $\mathcal{L}^T$. If the eigenvalues are as close to zero as for $|\rho_S\rangle$, we can conclude that we have a correct representation of the vacuum state. In our case, this approach always works because we drive the system only at one site so that $|\rho_S\rangle$ has a large component in the $|0\rangle$ direction.

Using DMRG, we find that in the presence of the interactions, the simple results for the expectation values (E1)–(E3) are no longer valid. Instead, the steady state of the interacting system is a correlated quantum state with entanglement between the transmons. As an example, we show in Fig. 5(c) that the relation (E2) is not satisfied in the interacting system. Here we have used the convergence parameters $r = 30$ and $d = 4$ for $U/J =: 0, 1, 2, 3$ and $d = 5$ for $U/J = 4$. With these parameters, we were able to keep the eigenvalue of the stationary state below $10^{-9}J$. Here we also present the reflection coefficients $|\Gamma_{11}(\omega)|$ beyond the linear response for $U/J =: 0, 1, 2, 3, 4$ (see Fig. 6), demonstrating that a satellite dip appears at $\omega \approx \omega_0 - nU/2$ and the main dip shifts slightly away from $\omega = \omega_0$ position. The other elements of the reflection matrix $|\Gamma_{1i}(\omega)|$ are shown in Fig. 7.

APPENDIX G: TIME EVOLUTION OF THE DENSITY MATRIX

Our starting point in the consideration of the dynamics is the Lindblad master equation in the absence of driving and interactions, but allowing time dependence of the parameters so that the dissipation can be switched on and off as discussed in the main text. Using the third-quantized operators, it can be written as

$$\begin{aligned} \frac{d}{dt}\rho(t) &= \mathcal{L}(t)\rho(t), \\ \mathcal{L}(t) &= -i(\vec{a}_0')^T H_{NH}(t)\vec{a}_0 + i(\vec{a}_1')^T \hat{H}_{NH}^*(t)\vec{a}_1. \end{aligned} \tag{G1}$$

The solution of Eq. (G2) can be written as

$$\begin{aligned} \rho(t) &= \mathcal{T}\exp\left[\int_0^t dt'\mathcal{L}(t')\right]\rho(0) \\ &= \mathcal{T}\exp\left[-i\int_0^t dt'(\vec{a}_0')^T \hat{H}_{NH}(t')\vec{a}_0\right]\mathcal{T} \\ &\quad \times \exp\left[i\int_0^t dt'(\vec{a}_1')^T \hat{H}_{NH}^*(t')\vec{a}_1\right]\rho(0), \end{aligned} \tag{G2}$$

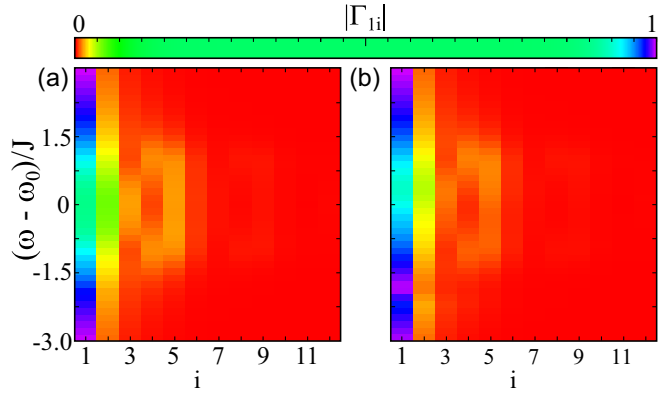

FIG. 7. Reflection and transmission coefficients $|\Gamma_{1i}(\omega)|$ in the nonlinear response regime as a function of frequency ω in the nontrivial phase ($x = -1$) for (a) $U/J = 1$ and (b) $U/J = 4$. The driving strength is $|f| = 0.4J$. Note that we have chosen a very nonlinear color-map scale because $|\Gamma_{1i}(\omega)|$ is close to 1 for $i = 1$ and close to 0 for $i \geqslant 2$ for all ω.

where $\mathcal{T}$ is the time-ordering operator. By applying this time evolution to an initial coherent state in the third-quantized operator representation of the density matrix,

$$\rho_{\vec{z}}(0) = \rho_{\vec{z}_0,\vec{z}_1}(0) = \exp\left[\vec{z}_0^T\vec{a}_0' + \vec{z}_1^T\vec{a}_1'\right]\rho_0, \tag{G3}$$

we obtain

$$\rho_{\vec{z}}(t) = \exp\left\{\vec{z}_0^T\hat{U}(t)\vec{a}_0' + \vec{z}_1^T\hat{U}^*(t)\vec{a}_1'\right\}\rho_0, \tag{G4}$$

where

$$\hat{U}(t) = \mathcal{T}\exp\left[-i\int_0^t dt'\hat{H}_{NH}(t')\right]. \tag{G5}$$

Thus, the sitewise product of the coherent states keeps this structure under time evolution. Therefore, we can straightforwardly evaluate the time-dependent expectation values of operators once we have an expansion of the initial state $\rho(0)$ in terms of the coherent states $\rho_{\vec{z}}(0)$.

If the state of the transmons is initialized into a sitewise product of coherent states in the second-quantized formalism, the corresponding density matrix translates into a sitewise product of coherent states also in the third-quantized formalism. Since this structure is kept during the time evolution, there is no entanglement between the transmons developing as a function of time.

As discussed in the main text, another possibility is to initialize one of the transmons into a Fock state in the second-quantized formalism. The Fock state density matrix $\rho_{n_i}(0) = \frac{1}{n!}(a_i^\dagger)^n|0\rangle\langle 0|a_i^n$ in the third-quantized formalism can be expressed as

$$\rho_{n_i}(0) = \frac{1}{n!}(a_{0,i}' + a_{1,i})^n(a_{0,i} + a_{1,i}')^n\rho_0 = \sum_{k=0}^n \frac{(a_{0,i}')^{n-k}a_{1,i}^k(a_{1,i}')^n}{k!(n-k)!}\rho_0 = \sum_{k=0}^n \frac{n!}{k!(n-k)!}|(n-k)_{0,i}(n-k)_{1,i}\rangle, \tag{G6}$$

and, after expressing this with the help of the coherent states, we obtain the time-dependent density matrix,

$$\rho_{n_i}(t) = \frac{1}{\pi^2}\sum_{k=0}^n \frac{n!}{k!(n-k)!}\int d^2z_{0,i}\int d^2z_{1,i}e^{-|z_{1,i}|^2-|z_{1,i}|^2}\frac{z_{0,i}^{\star(n-k)}z_{1,i}^{\star(n-k)}}{(n-k)!}\rho_{\vec{z}^{(i)}}(t), \quad \vec{z}_{0,k}^{(i)} = \delta_{i,k}z_{0,i} \;\; \vec{z}_{1,k}^{(i)} = \delta_{i,k}z_{1,i}. \tag{G7}$$

We are interested in the nonlocal entanglement between the transmons 1 and L, and therefore we compute the reduced density matrix by taking the partial trace of $\rho_{n_i}(t)$ over the other transmons,

$$\begin{aligned}\rho_{n_i}^{\mathrm{red}}(t) &= \frac{1}{\pi^2}\sum_{k=0}^n \frac{n!}{k!(n-k)!}\int d^2z_{0,i}\int d^2z_{1,i}e^{-|z_{1,i}|^2-|z_{1,i}|^2}\frac{z_{0,i}^{\star(n-k)}z_{1,i}^{\star(n-k)}}{(n-k)!}e^{z_{0,i}\hat{U}_{i1}a_{0,1}'}e^{z_{1,i}\hat{U}_{i1}^*a_{1,1}'}e^{z_{0,i}\hat{U}_{iL}a_{0,L}'}e^{z_{1,i}\hat{U}_{iL}^*a_{1,L}'}\rho_0 \\ &= \sum_{k=0}^n \frac{n!}{(n-k)!}\frac{1}{k!^2}\left(\hat{U}_{1i}a_{0,1}' + \hat{U}_{Li}a_{0,L}'\right)^k\left(\hat{U}_{1i}^*a_{1,1}' + \hat{U}_{Li}^*a_{1,L}'\right)^k\rho_0.\end{aligned} \tag{G8}$$

In the second-quantized form, this density matrix can be written as

$$\begin{aligned}\rho_{n_i}^{\mathrm{red}}(t) &= \sum_{k=0}^n \frac{n!}{(n-k)!}\frac{1}{k!^2}\left[\hat{U}_{1i}\left(a_1^{L\dagger} - a_1^{R\dagger}\right) + \hat{U}_{Li}\left(a_L^{L\dagger} - a_L^{R\dagger}\right)\right]^k|0\rangle\langle 0|[\hat{U}_{1i}^*a_1 + \hat{U}_{Li}^*a_L]^k \\ &= \sum_{k=0}^n \frac{n!}{(n-k)!}\frac{1}{k!^2}\sum_{p=0}^k \frac{k!}{p!(k-p)!}[\hat{U}_{1i}a_1^\dagger + \hat{U}_{Li}a_L^\dagger]^{k-p}|0\rangle\langle 0|\left[\hat{U}_{1i}^*a_1 + \hat{U}_{Li}^*a_L\right]^k\left[-\hat{U}_{1i}a_1^\dagger - \hat{U}_{Li}a_L^\dagger\right]^p \\ &= \sum_{k=0}^n \frac{n!}{(n-k)!}\sum_{p=0}^k \frac{1}{p!(k-p)!}(-1)^p(P_{1,i}+P_{L,i})^k|(k-p)_u\rangle\langle(k-p)_u| = \sum_{q=0}^n A_q|q_u\rangle\langle q_u|,\end{aligned} \tag{G9}$$

where

$$A_q = (1-P_{1,i}-P_{L,i})^{n-q}(P_{1,i}+P_{L,i})^q\binom{n}{q}, \quad |q_u\rangle = \frac{(\hat{U}_{1i}a_1^\dagger + \hat{U}_{Li}a_L^\dagger)^q}{\sqrt{q!(P_{1,i}+P_{L,i})^q}}|0\rangle, \quad P_{1,i} = |\hat{U}_{1i}|^2, \quad P_{L,i} = |\hat{U}_{Li}|^2. \tag{G10}$$

Similarly, we can also compute the reduced density matrix for a single transmon at one end of the chain,

$$\rho_{n_i}^{\mathrm{red},1}(t) = \sum_{p=0}^n B_{1,p}|p\rangle_1\langle p|_1, \;\; \rho_{n_i}^{\mathrm{red,L}}(t) = \sum_{p=0}^n B_{L,p}|p\rangle_1\langle p|_1, \;\; B_{1(L),p} = (P_{1(L),i})^p(1-P_{1(L),i})^{n-p}\binom{n}{p}. \tag{G11}$$

APPENDIX H: NONLOCAL ENTANGLEMENT

We can characterize the entanglement between the sites 1 and L in the reduced density matrix (G9) using different measures of entanglement. In the main text, we concentrated on the mutual information $I(1:L)$, which is defined as

$$I(1:L)(t) = S\left[\rho_{n_i}^{\mathrm{red},1}(t)\right] + S\left[\rho_{n_i}^{\mathrm{red,L}}(t)\right] - S\left[\rho_{n_i}^{\mathrm{red}}(t)\right], \tag{H1}$$

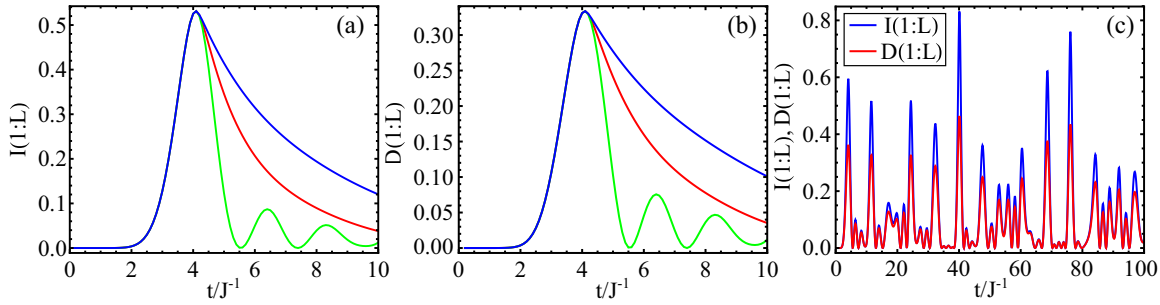

FIG. 8. (a) Mutual information $I(1:L)$ vs t for a reference system with $g_{B,\max} = 0.01J$ (green) and nontrivial phases with $x = -1$ and $g_{B,\max}/J =: 5, 10$ (red, blue). (b) Quantum discord $\delta(1:L)$ vs t for the same dissipation patterns. (c) Comparison of mutual information $I(1:L)$ and quantum discord $\delta(1:L)$ for a uniform system with no dissipation, $g_{A,B} = 0$. In addition to the usual dissipation patterns, we have added one extra site in the middle of the chain with $g_{L/2+1} = g_B$, which is excited to a Fock state with $N = 1$ at $t = 0$.

where $S(\rho)$ is the von Neumann entropy,

$$S(\rho) = -\mathrm{Tr}\rho \ln \rho. \tag{H2}$$

If the system is in a simple product state, we have $I(1:L) = 0$, and therefore the mutual information characterizes correlations between the end transmons.

By using Eqs. (G9) and (G11), we obtain

$$I(1:L)(t) = \sum_{q=0}^{n} A_q(t) \ln A_q(t) - \sum_{q=0}^{n} B_{1,q}(t) \ln B_{1,q}(t) - \sum_{q=0}^{n} B_{L,q}(t) \ln B_{L,q}(t), \tag{H3}$$

where $A_q(t)$, $B_{1,q}(t)$, and $B_{L,q}(t)$ are given by Eqs. (G10) and (G11). The formula (H3) has been used to compute the mutual information in the figures shown in the main text.

In general, the mutual information $I(1:L)$ is not a good measure of quantum entanglement because it can also be nonzero in the case of a classically correlated state. However, we have checked that in our case, the mutual information originates from the quantum entanglement. For this purpose, we have considered the quantum discord [54],

$$\delta(1:L)(t) = S\big[\rho_{n_i}^{\mathrm{red},1}(t)\big] - S\big[\rho_{n_i}^{\mathrm{red}}(t)\big] + S\big[\rho_{n_i}^{\mathrm{red,L}}(t)|\{\Pi_1^j\}\big], \tag{H4}$$

where the conditional quantum entropy is defined as

$$S\big[\rho_{n_i}^{\mathrm{red,L}}(t)|\{\Pi_1^j\}\big] = \sum_{j=0}^{n} p_j S\left[\frac{1}{p_j}\Pi_1^j \rho_{n_i}^{\mathrm{red}}(t)\Pi_1^j\right], \tag{H5}$$

p_j are the probabilities of the measurements,

$$p_j = \mathrm{Tr}\big\{\Pi_1^j \rho_{n_i}^{\mathrm{red}}(t)\big\}, \tag{H6}$$

and Π_1^j is a complete set of orthogonal projectors at site 1. Here, we concentrate on the case $n = 1$, where the projectors can be written as

$$\Pi_1^1 = (\cos\theta|0\rangle_1 + e^{i\phi}\sin\theta|1\rangle_1)(\cos\theta\langle 0|_1 + e^{-i\phi}\sin\theta\langle 1|_1), \tag{H7}$$

$$\Pi_1^2 = (e^{-i\phi}\sin\theta|0\rangle_1 - \cos\theta|1\rangle_1)(e^{i\phi}\sin\theta\langle 0|_1 - \cos\theta\langle 1|_1). \tag{H8}$$

In general, the discord depends on the basis taken to make the measurement at site 1, i.e., on the values of θ and ϕ in Eqs. (H7) and (H8), and therefore a meaningful measure of entanglement is

$$D = \min_{\{\Pi_j^1\}} \delta(1:L).$$

For $n = 1$, this means minimization over angles θ and ϕ, which is numerically feasible. We numerically find that in our case, dependence on the choice of $\{\Pi_j^1\}$ is weak and D shows very similar behavior as $I(1:L)$. In Fig. 8, we show the comparison between these two quantities in the case of time-dependent dissipation, which was already considered in the main text and in the case of no dissipation at all. We note that quantum discord always takes slightly lower or the same values as mutual information, but the shape of the curves is the same. In the main text, we have reported only $I(1:L)$ because of the rather high complexity of the calculation of D in the case of a large number of bosons.

APPENDIX I: INITIALIZATION AND MEASUREMENT WITH CIRCUIT QUANTUM ELECTRODYNAMICS

In this section, we will briefly review the initialization and measurement of the transmons with circuit quantum electrodynamics based on Refs. [33,51]. For this purpose, we consider our transmon chain coupled resonant mode of a cavity,

$$\mathcal{H}_{\mathrm{cqe}} = \vec{a}^\dagger \hat{H} \vec{a} - \sum_{j=1}^{L} \frac{U_j}{2} a_j^\dagger a_j (a_j^\dagger a_j - 1) + \omega_c c^\dagger c + \sum_j \mathcal{G}_j (c^\dagger a_j + c a_j^\dagger), \tag{I1}$$

where

$$\hat{H} = \begin{pmatrix} \omega_1 & J_1 & & & \\ J_1 & \omega_2 & J_2 & & \\ & J_2 & \ddots & \ddots & \\ & & \ddots & & J_{L-1} \\ & & & J_{L-1} & \omega_L \end{pmatrix}, \tag{I2}$$

and $\mathcal{G}_j$ describes the coupling of the transmon j and the cavity mode. The transmon frequencies ω_i can be tuned as much as 1 GHz in as little as 10–20 ns [51]. Therefore, we can assume that all transmon frequencies are, most of the time, tuned very far away from the cavity frequency ω_c, but we can selectively tune specific transmon frequencies close to the cavity frequency ω_c so that the coupling between these systems becomes non-negligible. Notice that even when ω_i is tuned close to ω_c, we will still stay in the dispersive regime $\omega_i - \omega_c - nU \ll \mathcal{G}_i$ $(n = 0, 1, \ldots, n_{\max}$, where the state-dependent cutoff occupation number $n_{\max}$ is defined so that as a good approximation, the occupations above $n_{\max}$ can be neglected). However, the other transmons are detuned so much more away from ω_c that their effects can be completely neglected. We also assume that J_j are sufficiently small so that while transmons are tuned close to ω_c, the couplings to the other transmons can be neglected. Therefore, we assume that during these operations, the dissipations g_i are always turned off.

1. Initialization and measurement of the state of a single transmon

We first consider a single transmon frequency ω_i tuned close to ω_c. In this case, the effective Hamiltonian describing the transmon and the cavity takes a form

$$\mathcal{H}_{\mathrm{cqe},i} = \omega_i a_i^\dagger a_i - \frac{U_i}{2} a_i^\dagger a_i (a_i^\dagger a_i - 1) + \omega_c c^\dagger c + \mathcal{G}_i (c^\dagger a_i + c a_i^\dagger). \tag{I3}$$

In the dispersive limit, one can utilize the Schrieffer-Wolff transformation [51] to show that the Hamiltonian (I3) is well approximated by

$$\mathcal{H}_{\mathrm{disp},i} = \omega_i a_i^\dagger a_i - \frac{U_i}{2} a_i^\dagger a_i (a_i^\dagger a_i - 1) + \omega_c c^\dagger c + \frac{\mathcal{G}_i^2\, a_i^\dagger a_i}{\omega_i - \omega_c - U_i (a_i^\dagger a_i - 1)} + \left[\frac{\mathcal{G}_i^2\, a_i^\dagger a_i}{\omega_i - \omega_c - U_i (a_i^\dagger a_i - 1)} - \frac{\mathcal{G}_i^2\, (a_i^\dagger a_i + 1)}{\omega_i - \omega_c - U_i a_i^\dagger a_i} \right] c^\dagger c. \tag{I4}$$

Therefore, the resonator frequency is renormalized so that it is dependent on the Fock state n of the transmon as

$$\omega_c^{\mathrm{eff}}(n) = \omega_c + \frac{n\mathcal{G}_i^2}{\omega_i - \omega_c - (n-1)U_i} - \frac{(n+1)\mathcal{G}_i^2}{\omega_i - \omega_c - nU_i} = \omega_c - \frac{\mathcal{G}_i^2 (\omega_i - \omega_c + U_i)}{(\omega_i - \omega_c - nU_i)[\omega_i - \omega_c - (n-1)U_i]}. \tag{I5}$$

In this situation, initializing the transmon to a superposition of the Fock states $|n\rangle$,

$$|\psi_{\mathrm{transmon}}\rangle = \sum_{n=0}^{n_{\max}} c_n |n\rangle, \tag{I6}$$

and driving the cavity leads to an entangled transmon-resonator state of the form

$$|\psi\rangle = \sum_{n=0}^{n_{\max}} c_n |n, \alpha_n\rangle, \tag{I7}$$

where α_n describes the transmon-state n-dependent coherent state of the resonator. Assuming that $\omega_c^{\mathrm{eff}}(n)$ $(n = 0, 1, \ldots, n_{\max})$ are sufficiently different from each other, the different states of the microwave field α_n can be resolved in heterodyne detection, and this measurement serves as a quantum nondemolition measurement of $\hat{n} = a^\dagger a$. Thus the transmon is projected in the measurement to the Fock state $|n\rangle$ with probability $|c_n|^2$. In the case of the two lowest states of the transmons, the measurement can be done with above 99% fidelity in less than 100 ns [51]. In the case of multiple states of the transmon $|n\rangle$ $(n = 0, 1, \ldots, n_{\max})$, we expect the fidelities to be smaller and the required measurement times to be longer.

Alternatively, one can also initialize the transmon to a chosen excited state utilizing the anharmonicity U_i. Namely, the frequency difference between states $|n\rangle$ and $|n+1\rangle$ is different for each value of n, and therefore one can sequentially apply π pulses at the corresponding resonance frequencies to go from the ground state to a chosen excited state $|0\rangle \to |1\rangle \to \cdots \to |n\rangle$ [52].

2. Two-transmon tomography

After we have dynamically generated the entangled state, the reduced density matrix of the transmons 1 and L can be experimentally determined by using quantum state tomography, but it requires that we prepare the transmons 1 and L to the same state many times by repeating the same procedure. For this purpose, we also always need to decouple the transmons 1 and L from the rest of the chain by tuning the resonance frequencies ω_1 and ω_L sufficiently far from the resonance frequencies of the other transmons.

The quantum state tomography can then be performed by applying single transmon gates and correlating the single transmon measurements of the transmons 1 and L. In the case of two-level systems, the typical approach is to measure the probabilities of the qubits being in states $|0\rangle$ and $|1\rangle$, e.g., in the x, y, and z basis; then the density matrix is constructed using the maximum-likelihood estimation of ρ (see, e.g., [55,56]). This method can be easily generalized to our case by noticing that we can formally express the states of the transmon $|n\rangle$ as tensor products of qubit states. The single transmon operations and measurements can be performed, for example, by driving the transmons with suitable pulses and utilizing the dispersive readout as discussed above.

Alternatively, the two-transmon tomography can be performed using joint dispersive readout [57]. In this scheme, one utilizes the Schrieffer-Wolff transformation for two qubits coupled to the same resonator, leading to the Hamiltonian

$$\mathcal{H}_{\mathrm{disp},1,L} = \omega_1 a_1^\dagger a_1 - \frac{U_1}{2} a_1^\dagger a_1 (a_1^\dagger a_1 - 1) + \omega_L a_L^\dagger a_L - \frac{U_L}{2} a_L^\dagger a_L (a_L^\dagger a_L - 1) + \omega_c c^\dagger c + \frac{\mathcal{G}_1^2\, a_1^\dagger a_1}{\omega_1 - \omega_c - U_1 (a_1^\dagger a_1 - 1)} + \frac{\mathcal{G}_L^2\, a_L^\dagger a_L}{\omega_L - \omega_c - U_L (a_L^\dagger a_L - 1)} + \left[\frac{\mathcal{G}_1^2\, a_1^\dagger a_1}{\omega_1 - \omega_c - U_1 (a_1^\dagger a_1 - 1)} - \frac{\mathcal{G}_1^2\, (a_1^\dagger a_1 + 1)}{\omega_1 - \omega_c - U_1 a_1^\dagger a_1} + \frac{\mathcal{G}_L^2\, a_L^\dagger a_L}{\omega_L - \omega_c - U_L (a_L^\dagger a_L - 1)} - \frac{\mathcal{G}_L^2\, (a_L^\dagger a_L + 1)}{\omega_L - \omega_c - U_L a_L^\dagger a_L} \right] c^\dagger c, \quad \text{(I8)}$$

in the dispersive limit. Because the renormalized resonator frequency is now dependent on the state of both transmons, the quadratures of the resonator field correspond to an operator which also comprises two-transmon correlation terms [57]. Therefore, it is possible to construct the density matrix by performing single transmon operations and the averaged measurements of the transmission amplitudes without the need for single-shot readout of individual transmons [57].

[1] R. El-Ganainy, K. G. Makris, M. Khajavikhan, Z. H. Musslimani, S. Rotter, and D. N. Christodoulides, Non-Hermitian physics and PT symmetry, Nat. Phys. **14**, 11 (2018).

[2] Z. Gong, Y. Ashida, K. Kawabata, K. Takasan, S. Higashikawa, and M. Ueda, Topological Phases of Non-Hermitian Systems, Phys. Rev. X **8**, 031079 (2018).

[3] S. Lieu, Topological symmetry classes for non-Hermitian models and connections to the bosonic Bogoliubov–de Gennes equation, Phys. Rev. B **98**, 115135 (2018).

[4] H. Zhou and J. Y. Lee, Periodic table for topological bands with non-Hermitian symmetries, Phys. Rev. B **99**, 235112 (2019).

[5] K. Kawabata, K. Shiozaki, M. Ueda, and M. Sato, Symmetry and Topology in Non-Hermitian Physics, Phys. Rev. X **9**, 041015 (2019).

[6] F. Song, S. Yao, and Z. Wang, Non-Hermitian Skin Effect and Chiral Damping in Open Quantum Systems, Phys. Rev. Lett. **123**, 170401 (2019).

[7] W. Brzezicki and T. Hyart, Hidden Chern number in one-dimensional non-Hermitian chiral-symmetric systems, Phys. Rev. B **100**, 161105(R) (2019).

[8] S. Lieu, M. McGinley, and N. R. Cooper, Tenfold Way for Quadratic Lindbladians, Phys. Rev. Lett. **124**, 040401 (2020).

[9] Y. Ashida, Z. Gong, and M. Ueda, Non-Hermitian physics, Adv. Phys. **69**, 249 (2020).

[10] E. J. Bergholtz, J. C. Budich, and F. K. Kunst, Exceptional topology of non-Hermitian systems, Rev. Mod. Phys. **93**, 015005 (2021).

[11] D. I. Pikulin and Y. V. Nazarov, Topological properties of superconducting junctions, JETP Lett. **94**, 693 (2012).

[12] D. I. Pikulin and Y. V. Nazarov, Two types of topological transitions in finite Majorana wires, Phys. Rev. B **87**, 235421 (2013).

[13] S. Mi, D. I. Pikulin, M. Marciani, and C. W. J. Beenakker, X-shaped and Y-shaped Andreev resonance profiles in a superconducting quantum dot, J. Expt. Theor. Phys. **119**, 1018 (2014).

[14] P. San-Jose, J. Cayao, E. Prada, and R. Aguado, Majorana bound states from exceptional points in nontopological superconductors, Sci. Rep. **6**, 21427 (2016).

[15] J. Avila, F. Peñaranda, E. Prada, P. San-Jose, and R. Aguado, Non-Hermitian topology as a unifying framework for the Andreev versus Majorana states controversy, Commun. Phys. **2**, 133 (2019).

[16] E. J. Bergholtz and J. C. Budich, Non-Hermitian Weyl physics in topological insulator ferromagnet junctions, Phys. Rev. Res. **1**, 012003(R) (2019).

[17] T. Hyart and J. L. Lado, Non-Hermitian many-body topological excitations in interacting quantum dots, Phys. Rev. Res. **4**, L012006 (2022).

[18] J. Cayao and A. M. Black-Schaffer, Exceptional odd-frequency pairing in non-Hermitian superconducting systems, Phys. Rev. B **105**, 094502 (2022).

[19] J. Cayao and A. M. Black-Schaffer, Bulk Bogoliubov Fermi arcs in non-Hermitian superconducting systems, arXiv:2208.05372.

[20] P. Comaron, V. Shahnazaryan, W. Brzezicki, T. Hyart, and M. Matuszewski, Non-Hermitian topological end-mode lasing in polariton systems, Phys. Rev. Res. **2**, 022051(R) (2020).

[21] T. Ozawa, H. M. Price, A. Amo, N. Goldman, M. Hafezi, L. Lu, M. C. Rechtsman, D. Schuster, J. Simon, O. Zilberberg, and I. Carusotto, Topological photonics, Rev. Mod. Phys. **91**, 015006 (2019).

[22] J. M. Zeuner, M. C. Rechtsman, Y. Plotnik, Y. Lumer, S. Nolte, M. S. Rudner, M. Segev, and A. Szameit, Observation of a Topological Transition in the Bulk of a Non-Hermitian System, Phys. Rev. Lett. **115**, 040402 (2015).

[23] C. Poli, M. Bellec, U. Kuhl, F. Mortessagne, and H. Schomerus, Selective enhancement of topologically induced interface states in a dielectric resonator chain, Nat. Commun. **6**, 6710 (2015).

[24] X. Zhan, L. Xiao, Z. Bian, K. Wang, X. Qiu, B. C. Sanders, W. Yi, and P. Xue, Detecting Topological Invariants in Nonunitary Discrete-Time Quantum Walks, Phys. Rev. Lett. **119**, 130501 (2017).

[25] L. Xiao, X. Zhan, Z. H. Bian, K. K. Wang, X. Zhang, X. P. Wang, J. Li, K. Mochizuki, D. Kim, N. Kawakami, W. Yi, H. Obuse, B. C. Sanders, and P. Xue, Observation of topological edge states in parity-time-symmetric quantum walks, Nat. Phys. **13**, 1117 (2017).

[26] S. Weimann, M. Kremer, Y. Plotnik, Y. Lumer, S. Nolte, K. G. Makris, M. Segev, M. C. Rechtsman, and A. Szameit, Topologically protected bound states in photonic parity–time-symmetric crystals, Nat. Mater. **16**, 433 (2017).

[27] H. Zhao, P. Miao, M. H. Teimourpour, S. Malzard, R. El-Ganainy, H. Schomerus, and L. Feng, Topological hybrid silicon microlasers, Nat. Commun. **9**, 981 (2018).

[28] M. A. Bandres, S. Wittek, G. Harari, M. Parto, J. Ren, M. Segev, D. N. Christodoulides, and M. Khajavikhan, Topological insulator laser: Experiments, Science **359**, 6381 (2018).

[29] M. Parto, S. Wittek, H. Hodaei, G. Harari, M. A. Bandres, J. Ren, M. C. Rechtsman, M. Segev, D. N. Christodoulides, and M. Khajavikhan, Edge-Mode Lasing in 1D Topological Active Arrays, Phys. Rev. Lett. **120**, 113901 (2018).

[30] T. Helbig, T. Hofmann, S. Imhof, M. Abdelghany, T. Kiessling, L. W. Molenkamp, C. H. Lee, A. Szameit, M. Greiter, and R. Thomale, Generalized bulk–boundary correspondence in non-Hermitian topo-electrical circuits, Nat. Phys. **16**, 747 (2020).

[31] P. A. McClarty and J. G. Rau, Non-Hermitian topology of spontaneous magnon decay, Phys. Rev. B **100**, 100405(R) (2019).

[32] Q. Liang, D. Xie, Z. Dong, H. Li, H. Li, B. Gadway, W. Yi, and B. Yan, Dynamic Signatures of Non-Hermitian Skin Effect and Topology in Ultracold Atoms, Phys. Rev. Lett. **129**, 070401 (2022).

[33] J. Koch, T. M. Yu, J. Gambetta, A. A. Houck, D. I. Schuster, J. Majer, A. Blais, M. H. Devoret, S. M. Girvin, and R. J. Schoelkopf, Charge-insensitive qubit design derived from the Cooper pair box, Phys. Rev. A **76**, 042319 (2007).

[34] F. Arute, K. Arya, R. Babbush, D. Bacon, J. C. Bardin, R. Barends, R. Biswas, S. Boixo, F. G. S. L. Brandao, D. A. Buell, B. Burkett, Y. Chen, Z. Chen, B. Chiaro, R. Collins, W. Courtney, A. Dunsworth, E. Farhi, B. Foxen, A. Fowler *et al.*, Quantum supremacy using a programmable superconducting processor, Nature (London) **574**, 505 (2019).

[35] Z. Chen, K. J. Satzinger, J. Atalaya, A. N. Korotkov, A. Dunsworth, D. Sank, C. Quintana, M. McEwen, R. Barends, P. V. Klimov, S. Hong, C. Jones, A. Petukhov, D. Kafri, S. Demura, B. Burkett, C. Gidney, A. G. Fowler, A. Paler, H. Putterman *et al.*, Exponential suppression of bit or phase errors with cyclic error correction, Nature (London) **595**, 600 (2021).

[36] S. Krinner, N. Lacroix, A. Remm, A. Di Paolo, E. Genois, C. Leroux, C. Hellings, S. Lazar, F. Swiadek, J. Herrmann, G. J. Norris, C. K. Andersen, M. Müller, A. Blais, C. Eichler, and A. Wallraff, Realizing repeated quantum error correction in a distance-three surface code, Nature (London) **605**, 669 (2022).

[37] Y. Zhao, Y. Ye, H.-L. Huang, Y. Zhang, D. Wu, H. Guan, Q. Zhu, Z. Wei, T. He, S. Cao, F. Chen, T.-H. Chung, H. Deng, D. Fan, M. Gong, C. Guo, S. Guo, L. Han, N. Li, S. Li *et al.*, Realization of an Error-Correcting Surface Code with Superconducting Qubits, Phys. Rev. Lett. **129**, 030501 (2022).

[38] C. Neill, T. McCourt, X. Mi, Z. Jiang, M. Y. Niu, W. Mruczkiewicz, I. Aleiner, F. Arute, K. Arya, J. Atalaya, R. Babbush, J. C. Bardin, R. Barends, A. Bengtsson, A. Bourassa, M. Broughton, B. B. Buckley, D. A. Buell, B. Burkett, N. Bushnell *et al.*, Accurately computing the electronic properties of a quantum ring, Nature (London) **594**, 508 (2021).

[39] K. J. Satzinger, Y.-J. Liu, A. Smith, C. Knapp, M. Newman, C. Jones, Z. Chen, C. Quintana, X. Mi, A. Dunsworth, C. Gidney, I. Aleiner, F. Arute, K. Arya, J. Atalaya, R. Babbush, J. C. Bardin, R. Barends, J. Basso, A. Bengtsson *et al.*, Realizing topologically ordered states on a quantum processor, Science **374**, 1237 (2021).

[40] X. Mi, M. Sonner, M. Yuezhen Niu, K. W. Lee, B. Foxen, R. Acharya, I. Aleiner, T. I. Andersen, F. Arute, K. Arya, A. Asfaw, J. Atalaya, R. Babbush, D. Bacon, J. C. Bardin, J. Basso, A. Bengtsson, G. Bortoli, A. Bourassa, L. Brill *et al.*, Noise-resilient Majorana Edge Modes on a Chain of Superconducting Qubits, Science **378**, 785 (2022).

[41] M. Partanen, J. Goetz, K. Y. Tan, K. Kohvakka, V. Sevriuk, R. E. Lake, R. Kokkoniemi, J. Ikonen, D. Hazra, A. Mäkinen, E. Hyyppä, L. Grönberg, V. Vesterinen, M. Silveri, and M. Möttönen, Exceptional points in tunable superconducting resonators, Phys. Rev. B **100**, 134505 (2019).

[42] M. Silveri, S. Masuda, V. Sevriuk, K. Y. Tan, M. Jenei, E. Hyyppä, F. Hassler, M. Partanen, J. Goetz, R. E. Lake, L. Grönberg, and M. Möttönen, Broadband Lamb shift in an engineered quantum system, Nat. Phys. **15**, 533 (2019).

[43] V. A. Sevriuk, K. Y. Tan, E. Hyyppä, M. Silveri, M. Partanen, M. Jenei, S. Masuda, J. Goetz, V. Vesterinen, L. Grönberg, and M. Möttönen, Fast control of dissipation in a superconducting resonator, Appl. Phys. Lett. **115**, 082601 (2019).

[44] T. F. Mörstedt, A. Viitanen, V. Vadimov, V. Sevriuk, M. Partanen, E. Hyyppä, G. Catelani, M. Silveri, K. Y. Tan, and M. Möttönen, Recent developments in quantum-circuit refrigeration, Annal. Phys. **534**, 2100543 (2022).

[45] T. Orell, M. Zanner, M. L. Juan, A. Sharafiev, R. Albert, S. Oleschko, G. Kirchmair, and M. Silveri, Collective bosonic effects in an array of transmon devices, Phys. Rev. A **105**, 063701 (2022).

[46] K. Takata and M. Notomi, Photonic Topological Insulating Phase Induced Solely by Gain and Loss, Phys. Rev. Lett. **121**, 213902 (2018).

[47] T. Orell, A. A. Michailidis, M. Serbyn, and M. Silveri, Probing the many-body localization phase transition with superconducting circuits, Phys. Rev. B **100**, 134504 (2019).

[48] O. Mansikkamäki, S. Laine, and M. Silveri, Phases of the disordered Bose-Hubbard model with attractive interactions, Phys. Rev. B **103**, L220202 (2021).

[49] T. Prosen and T. H. Seligman, Quantization over boson operator spaces, J. Phys. A: Math. Theor. **43**, 392004 (2010).

[50] R. Ma, B. Saxberg, C. Owens, N. Leung, Y. Lu, J. Simon, and D. I. Schuster, A dissipatively stabilized Mott insulator of photons, Nature (London) **566**, 51 (2019).

[51] A. Blais, A. L. Grimsmo, S. M. Girvin, and A. Wallraff, Circuit quantum electrodynamics, Rev. Mod. Phys. **93**, 025005 (2021).

[52] S. S. Elder, C. S. Wang, P. Reinhold, C. T. Hann, K. S. Chou, B. J. Lester, S. Rosenblum, L. Frunzio, L. Jiang, and R. J. Schoelkopf, High-Fidelity Measurement of Qubits Encoded in Multilevel Superconducting Circuits, Phys. Rev. X **10**, 011001 (2020).

[53] A. E. Feiguin, The density matrix renormalization group and its time-dependent variants, AIP Conf. Proc. **1419**, 5 (2011).

[54] H. Ollivier and W. H. Zurek, Quantum Discord: A Measure of the Quantumness of Correlations, Phys. Rev. Lett. **88**, 017901 (2001).

[55] H. Häffner, W. Hänsel, C. F. Roos, J. Benhelm, D. Chek-al-kar, M. Chwalla, T. Körber, U. D. Rapol, M. Riebe, P. O. Schmidt, C. Becher, O. Gühne, W. Dür, and R. Blatt, Scalable multiparticle entanglement of trapped ions, Nature (London) **438**, 643 (2005).

[56] M. Steffen, M. Ansmann, R. C. Bialczak, N. Katz, E. Lucero, R. McDermott, M. Neeley, E. M. Weig, A. N. Cleland, and J. M. Martinis, Measurement of the entanglement of two superconducting qubits via state tomography, Science **313**, 1423 (2006).

[57] S. Filipp, P. Maurer, P. J. Leek, M. Baur, R. Bianchetti, J. M. Fink, M. Göppl, L. Steffen, J. M. Gambetta, A. Blais, and A. Wallraff, Two-Qubit State Tomography Using a Joint Dispersive Readout, Phys. Rev. Lett. **102**, 200402 (2009).